

Modeling and Estimation of Energy-Based Hyperelastic Objects

Eder Miguel^{1,2} David Miraut¹ Miguel A. Otaduy¹

¹URJC Madrid ²IST Austria

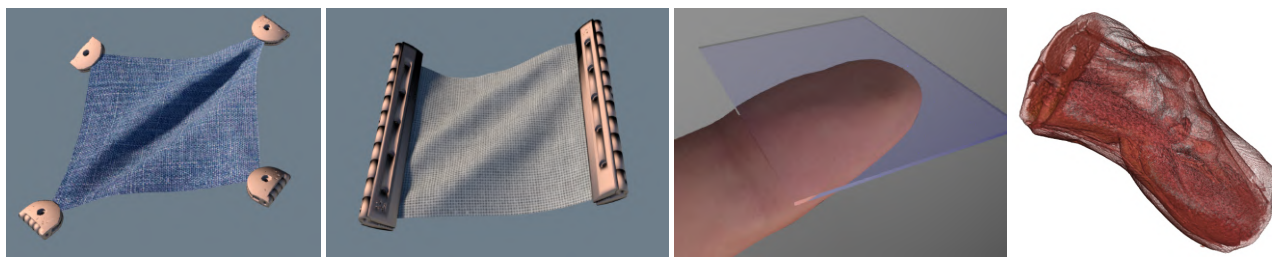


Figure 1: Deformations of real-world objects are nonlinear, anisotropic, and heterogeneous. Our general energy-based model of hyperelasticity allows the estimation of accurate and robust models for diverse real-world examples, including cloth, skin, or internal anatomy.

Abstract

In this paper, we present a method to model hyperelasticity that is well suited for representing the nonlinearity of real-world objects, as well as for estimating it from deformation examples. Previous approaches suffer several limitations, such as lack of integrability of elastic forces, failure to enforce energy convexity, lack of robustness of parameter estimation, or difficulty to model cross-modal effects. Our method avoids these problems by relying on a general energy-based definition of elastic properties. The accuracy of the resulting elastic model is maximized by defining an additive model of separable energy terms, which allow progressive parameter estimation. In addition, our method supports efficient modeling of extreme nonlinearities thanks to energy-limiting constraints. We combine our energy-based model with an optimization method to estimate model parameters from force-deformation examples, and we show successful modeling of diverse deformable objects, including cloth, human finger skin, and internal human anatomy in a medical imaging application.

Categories and Subject Descriptors (according to ACM CCS): I.3.7 [Computer Graphics]: Three-Dimensional Graphics and Realism—Animation

1. Introduction

A growing interest in computer graphics is to produce simulation models that match the elastic behavior of deformable objects in the real world. One possibility to reach this goal is to acquire example deformations of real objects, and estimate parameters of constitutive models that best match the acquired examples. Unfortunately, real materials show a high degree of complexity, in the form of heterogeneity, anisotropy, and nonlinearity. Several works in computer graphics have addressed this complexity by estimating strain-dependent stiffness parameters, both for volumetric solids [BBO*09] and for cloth [WOR11, MBT*12]. However, in the most general case, these methods fail to enforce a fundamental property of elasticity: estimated forces are not conservative.

In this work, we propose to model general hyperelastic materi-

als using separable energy addends. With this model, elastic forces are conservative by construction, and we also show how to enforce convexity of the total energy. We demonstrate that, with the right choice of energy terms and basis functions, our model can exactly match common standard models. But, extending such standard models, nonlinearity and heterogeneity are easily obtained by interpolating energy parameters in strain and material space respectively. And we also enable the efficient implementation of extreme nonlinearity by adding energy-limiting constraints to the model.

A major difficulty when trying to estimate the nonlinearity and heterogeneity of real-world objects is that the parameter space becomes high dimensional and contains local minima. Our additive energy model allows us to circumvent local minima during parameter estimation by progressively increasing the number of en-

ergy addends, nonlinearity control points, and heterogeneity control points. We have devised a general optimization procedure that takes as input real-world force-deformation examples and estimates energy parameters such that simulations match best the measured forces and deformations or other higher-level metrics (e.g., image similarity).

Our formulation is general and can be used to model a variety of real-world objects, including volumetric elastic objects and thin shells. In this paper, we show the application of our model to the estimation of complex nonlinearities in cloth, extreme nonlinearities of finger skin deformation, and combined mechanical model estimation and non-rigid registration of internal human anatomy in medical imaging data, as shown in Fig. 1.

2. Related Work

Simulation of elasticity has been a major research topic in computer graphics for several decades. Starting with the seminal paper by Terzopoulos et al. [TPBF87], a wide variety of elasticity models have been proposed. An approach of growing popularity to model volumetric solids or thin shells is to adapt continuum models borrowed from computational mechanics, and augment them with features to increase robustness and/or efficiency [MG04, ITF04, BJ05, GHDS03, BMF03, PMS12, NSO12].

Real-world elastic materials present many sources of complexity: hyperelasticity, hysteresis, plasticity, viscosity, or heterogeneity. In this work, we focus on modeling heterogeneous hyperelasticity. This is a topic of interest in computational mechanics as well, specially in biomechanics [GOH06]. Several constitutive models have been designed to capture accurately with few parameters the behavior of hyperelastic materials, such as the general Ogden model, or other variants like neo-Hookean or Mooney-Rivlin [Ogd97, BW97].

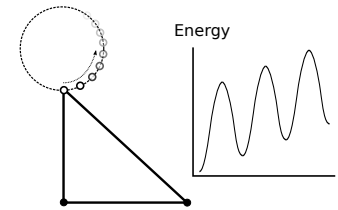
Several works in the past have attempted the estimation of material parameters of deformable objects. In biomechanics, Flynn et al. [FTN11] estimated parameters for hyperelastic models based on *in vivo* measurements of human skin. In computer graphics, the pioneering work of Pai et al. [PvdDJ*01] introduced a system to capture and estimate shape, elasticity, and surface roughness by scanning a volumetric object; Becker and Teschner [BT07] presented a method to estimate Young's modulus and Poisson ratio in a linear FEM formulation by solving a linear least squares problem; Bickel et al. [BBO*09] captured nonlinearity by interpolating stiffness parameters in strain space, and heterogeneity by defining such strain-space interpolation differently for each element along the material domain. Our work follows a similar sampling strategy for heterogeneity, but we capture nonlinearity with an energy model, not stiffness parameters.

For cloth, the traditional method to capture nonlinear elasticity has relied on the Kawabata Evaluation System (KES) [Kaw80]. Complex machinery is used to exert controllable uniform strain on cloth samples, and then estimate parameters of elastic models [BHW94, VMTF09]. Despite the complexity of the capture setup, KES suffers a major shortcoming: by exciting cloth with uniform strain it fails to capture the interplay between different deformation modes. Recent approaches exploit computer vision to cap-

ture arbitrary cloth deformations and then estimate model parameters. Bhat et al. [BTH*03] tried to extract model parameters from casually captured videos. More recently, Bouman et al. [BXXBF13] estimate cloth stiffness through the temporal analysis of texture patterns in video. Wang et al. [WOR11] and Miguel et al. [MBT*12] advocate for a combination of semi-controlled deformations and computer-vision-based tracking. Both teams estimate parameters of nonlinear models. Wang et al. estimate stiffness parameters that depend on the value and direction of the principal membrane strain. Miguel et al., on the other hand, compare strain-dependent stiffness parameters for individual deformation modes in several popular cloth models.

Despite the diversity of approaches, the majority of previous methods that model hyperelastic materials through parameter interpolation fail to enforce conservative forces. Previous works [BBO*09, WOR11] captured nonlinearities by making the coefficients of a linear strain-stress relationship strain-dependent, thus making the resulting model nonlinear. Unfortunately,

this choice makes forces non-integrable (and thus not conservative), as the stress is no longer guaranteed to be the derivative of some energy field. The inset shows an example of a triangle with two fixed vertices and the third one moved in circles. The plot shows the growing energy, computed as the work done to move the vertex with a Saint Venant-Kirchhoff (StVK) material model with strain-dependent Young's modulus $E = \epsilon_1 + 2\epsilon_2 + 3\epsilon_{12}$, where ϵ_1 and ϵ_2 are stretches, and ϵ_{12} is shear strain. With our energy-based parameterization of hyperelastic materials we achieve conservative forces by construction.



Another desirable property of elastic objects is that larger deformations produce larger forces. We achieve this by enforcing convexity of the total energy function. Not all standard nonlinear constitutive models enforce energy convexity explicitly. For example, the energy terms in the Ogden model [Ogd97] are defined as powers of principal stretches. There are no constraints on the values of these powers, and consequently the model may not be convex. On the other hand, Neo-Hookean models are defined by energy terms quadratic in the principal stretches, which makes them convex by definition. Polyconvexity would be a better choice, as convexity is an excessive constraint that prevents our model from capturing some real-world effects [MH83], but we found convexity to be a good compromise given that the design of polyconvex energy functions is still an issue in progress in mechanical engineering [ESN10].

A recent work by Xu et al. [XSZB15], developed concurrently to ours, succeeds to enforce conservative forces and energy convexity to materials that fulfill the Valanis-Landel hypothesis. Their focus is on user-editing of hyperelastic behaviors, mostly stiffening, not on measurement-based model estimation.

Even though our work is focused on the estimation of hyperelasticity, it is worth mentioning previous efforts on model esti-

mation for other relevant deformation effects. In particular, there are approaches aimed at estimating temporal effects of deformation due to viscoelasticity [SLS04], or even non-linear viscoelasticity [KVD*02], elasto-plastic behaviors [ZYZZ, PDP*15], irreversible deformations due to plasticity [KL04], or hysteresis produced by internal friction in cloth [MTB*13]. Sifakis et al. [SS-RMF06] went beyond the estimation of passive mechanical parameters, in particular facial muscle activation.

3. A General Model of Hyperelasticity

In this section, we present our model of hyperelasticity based on the addition of strain-dependent energy terms. We start with the formal definition of the additive energy model, followed by a description of strain-dependent energy addends. Then, we discuss the connections between our model and several standard hyperelasticity models as well. We continue with a description of the enforcement of energy convexity, heterogeneity, and the use of energy-limiting constraints. Finally, we conclude with remarks concerning the use of our model in the context of FEM simulations.

3.1. Additive Energy Model

The elastic forces of a hyperelastic material can be defined using a generic strain energy density function. Given a point \mathbf{X} in rest position, deformed to position \mathbf{x} , the deformation gradient is defined as $\mathbf{F} = \frac{\partial \mathbf{x}}{\partial \mathbf{X}}$. Then, the strain energy density can be defined as a generic function of the deformation gradient, $\Psi(\mathbf{X}) = f(\mathbf{F}(\mathbf{X}))$. Alternatively, we can express the energy density as a function of the Green strain tensor $\mathbf{E} = \frac{1}{2}(\mathbf{F}^T \mathbf{F} - \mathbf{I})$, i.e., $\Psi(\mathbf{X}) = f(\mathbf{E}(\mathbf{X}))$. Finally, elastic forces can be obtained by differentiating the integral of strain energy density. With an energy-based definition of the hyperelastic material, forces are integrable by construction.

The complete strain energy density depends on all terms of the strain tensor in a complex manner. To simplify the estimation of the complete energy, we propose an additive formulation:

$$\Psi(\mathbf{X}) = \sum_k \Psi_k(\mathbf{e}_k(\mathbf{X})), \quad (1)$$

where each Ψ_k depends on a different subset of the terms in the strain tensor, $\mathbf{e}_k = \{\mathbf{E}_{ij}\}$. In practice, we use unidimensional or bidimensional \mathbf{e}_k , capturing individual deformation components and interactions between two different deformation components, respectively. But the model allows for more complex interactions by increasing the strain terms on which the strain energy functions depend.

This formulation is very general and it can also represent popular hyperelastic models, such as StVK, Ogden, Neo-Hookean, or other invariant-based models [Ogd97]. For example, for the StVK model the energy addends are given by quadratic terms of the Green strain tensor, in the Ogden model they are given by various powers of principal stretches, and in the Neo-Hookean model the energy depends on the first invariant of the left Cauchy-Green strain tensor, which corresponds to the sum of squared principal stretches.

In computational mechanics, uncoupled formulations use a similar principle to separate strain energy into independent com-

ponents. Uncoupled formulations commonly separate volumetric (volume changing) and isochoric (volume preserving) components [MEAW12, LSF12], but they have also been used for components capturing transversely isotropic behaviors [WMG96, CDH01]. In contrast, our formulation is more general. It captures arbitrary non-linearities through the interpolated strain energy functions, and naturally extends to include other effects such as heterogeneity and constraints (which can include volume preservation). Most importantly, it is designed to accommodate a robust parameter estimation procedure thanks to the energy addends based on individual spatial deformation components.

3.2. Interpolated Energy Functions

We design each energy addend as the interpolation of energy samples in the addend-dependent strain domain:

$$\Psi_k(\mathbf{X}) = \sum_s \phi(\mathbf{e}_k(\mathbf{X}) - \mathbf{e}_k^{(s)}) \Psi_k^{(s)}, \quad (2)$$

where ϕ denotes some basis function, $\mathbf{e}_k^{(s)}$ a particular sample of the strain component \mathbf{e}_k and $\Psi_k^{(s)}$ its corresponding weight.

The choice of basis function allows us to obtain a diverse set of behaviors. For instance, we can replicate the StVK model. The strain energy density is formulated as $\Psi = \frac{\lambda}{2} \text{tr}(\mathbf{E})^2 + \mu \text{tr}(\mathbf{E}^2)$, with λ and μ Lamé parameters, and \mathbf{E} Green strain. In the 2D case, with stretches E_{11} and E_{22} and shear strain E_{12} , this strain energy density can be rewritten in an additive manner as:

$$\Psi = \underbrace{\left(\frac{\lambda}{2} + \mu\right) E_{11}^2}_{\Psi_1} + \underbrace{\left(\frac{\lambda}{2} + \mu\right) E_{22}^2}_{\Psi_2} + \underbrace{\lambda E_{11} E_{22}}_{\Psi_3} + \underbrace{2\mu E_{12}^2}_{\Psi_4}. \quad (3)$$

The energy addends Ψ_1 , Ψ_2 and Ψ_4 are unimodal and can be represented as quadratic energy addends (one quadratic basis function each). The addend Ψ_3 , on the other hand, is bimodal and can be represented using one bilinear basis function.

During data-driven parameter estimation, we use basis functions with local support. This way, each energy control point is influenced only by a fraction of the input data, thereby simplifying the structure of the optimization problem. Specifically, for unidimensional strain-energy density functions we use cubic Hermite splines with equidistant sample points, and for bidimensional components we use bilinear functions with a regular 3x3 grid of sample points. For high-dimensional strain domains, we propose clamped Gaussian radial basis functions to interpolate scattered control points.

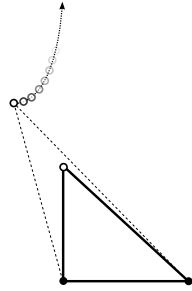
The power of our proposed additive model lies in its ability to naturally capture:

- Anisotropy, which could be added, e.g., to (3) simply by using different functions for the stretch energy addends Ψ_1 and Ψ_2 .
- Additional strain-dependencies (e.g., material hardening), which could be obtained by adding further control points to each energy addend.
- Cross-stiffening, which could be modeled with bimodal terms that relate stretch and shear.
- Volume/Area preservation or strain-limiting, which could be modeled as energy addends that weight the deviation w.r.t. default volume, area, or strain values. Patterson et al. [PMS12]

also formulate volume preservation as an energy addend. In Section 3.5 we show how to enforce hard deformation constraints using energy-limiting constraints.

3.3. Convexity

Convexity of the strain energy density function w.r.t. the deformation metric ensures that larger deformations lead to larger forces. As discussed in Section 2, the condition of energy convexity is too restrictive for some real-world effects, and should eventually be relaxed in favor of polyconvexity. Convexity also ensures stability of numerical integration under some choice of time step. Taking again as example the 2D StVK model in (3), the bimodal addend Ψ_3 , which captures area preservation, is concave. With a regular StVK model, enforcing convexity of the total energy is simple, as it reduces to imposing conditions on the Lamé parameters. The shear modulus μ is always positive, but a large negative value of λ can turn the energy concave along some direction. The inset shows a deformed triangle and the diverging motion due to large negative λ . With a strain-dependent model, energy convexity is more difficult to enforce, as it may be locally violated.



An energy function is convex iff the eigenvalues of its Hessian are always positive. For fully general energy functions this would require constraining the energy Hessian in the full strain domain. For bilinear addends, the Hessian is constant; while for cubically interpolated unimodal addends, it is piecewise linear. This allows us to limit the enforcement of a convex energy Hessian to the control points of the energy function. In Section 4.3, we describe the enforcement of convexity in the context of our optimization framework for parameter estimation.

3.4. Heterogeneity

We model heterogeneity by sampling the deformable object in material space at the desired resolution to capture material heterogeneity and define a separate additive energy model $\Psi^{(m)}$ at each sample point $\mathbf{X}^{(m)}$. Then, to obtain the strain energy density at an arbitrary test point \mathbf{X} in material space, we first evaluate energies at the sample points using the deformation at the test point \mathbf{X} , and then interpolate these energies using basis functions ϕ :

$$\Psi(\mathbf{X}) = \sum_m \phi(\|\mathbf{X} - \mathbf{X}^{(m)}\|) \Psi^{(m)}(\mathbf{X}). \quad (4)$$

In our examples, we have modeled heterogeneity using scattered energy samples in material space. In this case, we interpolate strain energy densities in material space using normalized Gaussian radial basis functions, but other interpolation strategies are also possible.

3.5. Energy-Limiting Constraints

Modeling extremely stiff materials using strain energy density functions requires the resolution of stiff systems of equations,

which usually requires tiny time steps and slows down the convergence rate of commonly used solvers.

As an alternative to stiff energy models, we propose to augment the additive energy model described so far with energy-limiting constraints. Several authors have enforced in the past constraints on strain [Pro95, GHF*07, TPS09, WOR10, PCH*13] or volume [ISF07] to model extreme nonlinearities. Other approaches, such as u - P formulations in biomechanics, are designed to address volume preservation. As a small variant, we express constraints on strain energy density, which allows us to constrain either individual addends, combinations, or the total energy. In general, energy-limiting constraints can be expressed as:

$$C = \Psi_{\max} - \Psi(\mathbf{X}) \geq 0. \quad (5)$$

3.6. FEM Simulation

In our examples, we have used FEM to discretize elastic deformation problems. We have tested tetrahedral elements with linear interpolation and hexahedral elements with trilinear interpolation. For an introduction to the implementation of FEM for elasticity problems, we refer the reader to the course by Sifakis and Barbic [SB12]. To compute elastic forces, we first integrate the strain energy densities over each element using quadrature points (1 point for tetrahedra and 8 points for hexahedra), and then differentiate these energies w.r.t. element nodes. Each strain energy density evaluation on a quadrature point requires: first, the evaluation of each energy addend for each nearby material sample, according to (2); second, the computation of the total energy for each nearby material sample, according to (1); and third, the interpolation of energies from material samples, according to (4). Energy-limiting constraints are evaluated and enforced on each quadrature point separately.

We have implemented elastic force computation using finite differences, which reduces to performing multiple evaluations of each element's strain energy (13 for tetrahedra and 25 for hexahedra). Implicit integration or (quasi-)static simulation also require the Hessian of the energy, which again we compute through finite differences of forces. Finite differences turn out computationally expensive compared to analytic derivatives, but they provide flexibility and simplify implementation, hence they are particularly attractive at the model design stage. Once the energy model is finalized, it is worth deriving analytic expressions of forces and their Jacobians for improved performance. Finite differences may also suffer robustness and inaccuracy problems, but this proved not to be an issue in our implementation.

4. Data-Driven Material Estimation

In this section, we describe an optimization framework for the estimation of material parameters in our energy model. Here, we assume that the parameter set is fixed, but the parameter set can be progressively refined to circumvent local minima. Later in Section 5, we discuss how we use this framework progressively in several applications with very diverse deformations and data, ranging from sparse to dense measurements.

Let us consider a general deformable object with a vector \mathbf{q} that

concatenates all its nodal positions, and a vector \mathbf{f} that concatenates all nodal forces. Our optimization framework receives as input a set of N example deformations in static equilibrium. Each of the example deformations is produced from some known boundary conditions (forces \mathbf{f}_c and/or positions \mathbf{q}_c), and contains some known measurements $\bar{\mathbf{m}}$. We consider diverse types of measurements, such as positions, forces, or image intensities.

Given a set of material parameters \mathbf{p} , consisting of energy control points, and their fixed positions in strain-space, the goal of the optimization framework is to estimate these parameters such that the least-squares error between the known measurements $\bar{\mathbf{m}}$ and their estimated values $\mathbf{m}(\mathbf{f}, \mathbf{q})$ is minimized, subject to static equilibrium and energy convexity. We formally define the objective function of the optimization by summing the error over all examples:

$$f_{obj} = \frac{1}{2} \sum_{i=1}^N w_i \|\mathbf{m}_i([\mathbf{q}_i, \mathbf{f}_i](\mathbf{p}, \mathbf{f}_{c,i}, \mathbf{q}_{c,i})) - \bar{\mathbf{m}}_i\|^2. \quad (6)$$

We enable the possibility to weight examples differently with $\{w_i\}$. In the expression above, we explicitly indicate that estimates of measured variables \mathbf{m} depend on simulated positions and forces, and through these they depend on estimated parameters and boundary conditions. Note that the measured variables and the nodes where boundary conditions are applied may differ across examples.

Our optimization framework iterates the following three steps until convergence:

1. Update the parameter set through local optimization.
2. Project parameters to enforce energy convexity.
3. Simulate all examples to static equilibrium.

Next, we discuss these three steps in detail.

4.1. Parameter Estimation

In each iteration of parameter estimation, we minimize (6) subject to energy convexity and static equilibrium. We treat these two types of constraints differently. We do not enforce energy convexity during parameter updates, and instead, we compute an unconstrained update and project the parameters to a convex configuration afterwards, as described in Section 4.3. On the other hand, we enforce static equilibrium implicitly during parameter updates. We do this by computing a Jacobian of positions w.r.t. parameters that respects static equilibrium. After the parameter update, it is anyway necessary to project all examples to static equilibrium, as they may have slightly deviated.

For each input example, we formulate the Jacobian of positions w.r.t. parameters $\frac{\partial \mathbf{q}_i}{\partial \mathbf{p}}$ through the application of the implicit function theorem on the static equilibrium constraints. In this case, we do not use finite differences to compute derivatives because evaluating positions for a new set of parameters requires solving a quasi-static problem, which is computationally expensive. In its most general formulation, our energy model includes energy-limiting constraints; therefore, static equilibrium forces include energy-limiting constraint forces: $\mathbf{f}_i + \mathbf{J}_i^T \alpha_i = \mathbf{0}$. In this expression, we assume that energy-limiting constraints are enforced through Lagrange multipliers, and $\mathbf{J}_i = \frac{\partial \mathbf{C}_i}{\partial \mathbf{q}_i}$ is the Jacobian of active energy-limiting constraints \mathbf{C}_i for the i^{th} example. We denote Lagrange multipliers as

α to avoid confusion with the Lamé constant λ . The enforcement of hard energy-limiting constraints complicates the application of the implicit function theorem, as it requires to first solve for Lagrange multipliers.

However, we observe that the purpose of the implicit function theorem is just to provide a suitable Jacobian of positions w.r.t. parameters. Then, for the computation of this Jacobian, we found that it is sufficient to approximate energy-limiting constraints as soft constraints with energy $\frac{1}{2} k \|\mathbf{C}\|^2$, for some large value of the stiffness k . Taking only active constraints, the static equilibrium in the i^{th} example can then be reformulated as:

$$\mathbf{f}_i - k \mathbf{J}_i^T \mathbf{C}_i = \mathbf{0}. \quad (7)$$

Differentiating the static equilibrium constraints (7) w.r.t. the vector of parameters, we obtain:

$$\frac{\partial \mathbf{f}_i}{\partial \mathbf{p}} - k \mathbf{J}_i^T \frac{\partial \mathbf{C}_i}{\partial \mathbf{p}} + \frac{\partial \mathbf{f}_i}{\partial \mathbf{q}_i} \frac{\partial \mathbf{q}_i}{\partial \mathbf{p}} - k \mathbf{J}_i^T \mathbf{J}_i \frac{\partial \mathbf{q}_i}{\partial \mathbf{p}} = \mathbf{0}. \quad (8)$$

And from this we obtain the Jacobian of positions w.r.t. parameters that satisfies equilibrium:

$$\frac{\partial \mathbf{q}_i}{\partial \mathbf{p}} = \left(\frac{\partial \mathbf{f}_i}{\partial \mathbf{q}_i} - k \mathbf{J}_i^T \mathbf{J}_i \right)^{-1} \left(\frac{\partial \mathbf{f}_i}{\partial \mathbf{p}} - k \mathbf{J}_i^T \frac{\partial \mathbf{C}_i}{\partial \mathbf{p}} \right). \quad (9)$$

In practice, we evaluate all terms in this expression using finite differences, but accounting for sparsity patterns for efficiency. If the energy model does not include energy-limiting constraints, it is sufficient to drop the related terms from the expression.

By enforcing static equilibrium constraints implicitly in the Jacobian of positions, the optimization problem (6) turns into an (unconstrained) nonlinear least-squares problem. We solve this problem iteratively using Gauss-Newton followed by a line-search. Gauss-Newton requires the evaluation of the derivative of the estimates of measurements \mathbf{m}_i , which can be written as:

$$\frac{\partial \mathbf{m}_i}{\partial \mathbf{p}} = \frac{\partial \mathbf{m}_i}{\partial \mathbf{q}_i} \frac{\partial \mathbf{q}_i}{\partial \mathbf{p}} + \frac{\partial \mathbf{m}_i}{\partial \mathbf{f}_i} \frac{\partial \mathbf{f}_i}{\partial \mathbf{p}}. \quad (10)$$

In this expression, we plug in the Jacobian of constrained positions (9). The Jacobians of estimates of measurements w.r.t. positions $\frac{\partial \mathbf{m}_i}{\partial \mathbf{q}_i}$ and w.r.t. forces $\frac{\partial \mathbf{m}_i}{\partial \mathbf{f}_i}$ are trivial when those measured variables are positions and/or forces, as is the case in some of our experiments. In cases where the measured variables depend in a complex way on simulated forces and positions, such as image intensity in one of our experiments, we opt to compute their derivatives w.r.t. the parameters directly through finite differences.

4.2. Static Equilibrium

After each update of material parameters, we reproject all input examples to static equilibrium. We use a different method depending on the type of deformable object and energy model.

For volumetric objects whose energy model does not contain energy-limiting constraints, we found that Newton-Raphson-type root-finding performs best. For thin shells (e.g., cloth) with no energy-limiting constraints, we found that dynamic relaxation with kinetic damping [Bar88, VMT07] performs best.

For objects with energy-limiting constraints, static equilibrium

should be posed as the minimization of potential energy (elastic plus gravitational) subject to the energy-limiting constraints. We found that, instead of imposing constraints on quasi-static iterative updates, we obtain better convergence by imposing constraints on regular dynamic simulations used during dynamic relaxation. For the enforcement of energy-limiting constraints in dynamic simulations, we use Lagrange multipliers and an LCP solver [CPS92], analogous to constraint-based solvers for contact problems.

4.3. Convex Energy Projection

We propose to enforce energy convexity on discrete samples of the strain domain. As discussed in Section 3.3, for the types of energy functions that we have used in our experiments, we simply enforce convexity on control points of the energy function. For heterogeneous models, this needs to be done for each material sample independently.

After an unconstrained parameter update, we test the convexity of the total energy on all control points. If some eigenvalue of the energy is negative at some control point, we project the parameter set along the gradient of the eigenvalue until it becomes positive. We implement this projection as an iterative search along the projection direction.

5. Results

We have tested our modeling and estimation framework on a variety of deformable objects and applications. Table 1 summarizes the main properties of each experiment. The cloth experiment contains dense, time-coherent data, while the finger and knee experiments contain very sparse data (4 and 3 example deformations, respectively). Each experiment allows us to test certain aspects of our approach, and altogether they allow us to validate its generality. All experiments were executed on a 2.67 GHz Intel Core i7 920 CPU with 12 GB RAM.

5.1. Cloth Models from Force-Deformation Data

For this experiment, we have used data captured by Miguel et al. [MBT*12], specifically data from two of their cloth samples (knit and denim). They applied slow controlled deformations on square cloth samples of 100 mm, measured the forces applied through cables, and captured 3D reconstructions of the deformed configurations.

Experiment	Finger	Cloth	Knee
Example deformations N	4	30 - 45	3
Size of position vector \mathbf{q}	360	893	762
Size of parameter set \mathbf{p}	2	22	8 - 32
Number of measurements \mathbf{m}	1	60 - 180	>1.0E6

Table 1: Size of the optimization problem for each experiment. The size of the position vector and the number of measurements refer to each example deformation. The size of the parameter set \mathbf{p} refers to the number of control points and/or energy constraint values optimized.

We discretize the cloth geometry using an irregular triangle mesh with 520 triangles, and solve the quasi-static problem for each frame using clip positions as boundary conditions. To formulate the objective function (6), we use as measured variables the positions of mesh vertices and the forces on clips attached to the cloth samples. We start with an isotropic StVK model for membrane deformations and the discrete shells model for bending [GHDS03], and then progressively increase the complexity:

1. Independent addends for stretch, shear and area preservation. Anisotropy is added to stretch through different addends for each deformation axis. Area preservation is modeled as a bidimensional energy added depending on warp and weft strain components.
2. Cross-modal stiffening between stretch and shear, as bidimensional addends depending on warp-shear, and weft-shear strain components.
3. Nonlinearity on stretch and shear, through strain-dependent energy interpolation using multiple control points.
4. Addends are made asymmetric.

We did not analyze complex modeling of bending energies. In order to place the control points, we perform a visual analysis of the input data to find the populated space of strains. After removing outliers, we set the initial control points to the boundaries of this space and progressively increase the number of points. Then, for nonlinear addends, we progressively add new control points equidistantly.

The training data consists of 30 to 45 keyframes of quasi-uniform stretch and shear deformation cycles. The test data consists of complex non-uniform deformations, denoted as *corner-pull* and *complex shear* (See Fig. 2). The figure also shows frames of the complex deformations simulated with our model and compared to the test data, as well as error visualizations comparing our full energy model and a regular StVK model. Table 2 shows the evolution of position and force RMS error as the energy model is augmented through the optimization scheme.

This dataset constitutes a challenge for a regular constitutive model due to the large nonlinearity, anisotropy, and often even asymmetry in cloth mechanics. This is evidenced by the progressive improvement of the fitting error as energy addends are included or refined, in particular for the denim sample. The complexity of the energy function that best describes the full hyperelastic behavior can also be observed in Fig. 3. This figure compares the energy function after estimating a regular StVK model and after estimating our final additive energy model. With our energy model, anisotropy, asymmetry, and strain-dependent nonlinearity are evident.

We also observed that error in the training data was often dominated by forces, not positions. This is expected given that the deformations are produced using positions as boundary conditions. And, as a result, the progressive improvement of the position error in the training datasets is almost negligible, in contrast to the force error. We also conjecture that the remaining force error might be dominated by cloth hysteresis, not captured by our model.

5.2. Internal Tissue Model and Image Registration

For this benchmark, we have used 3D MRI data of a knee obtained by Rhee et al. [RLNN11], which contains volumetric images for 4

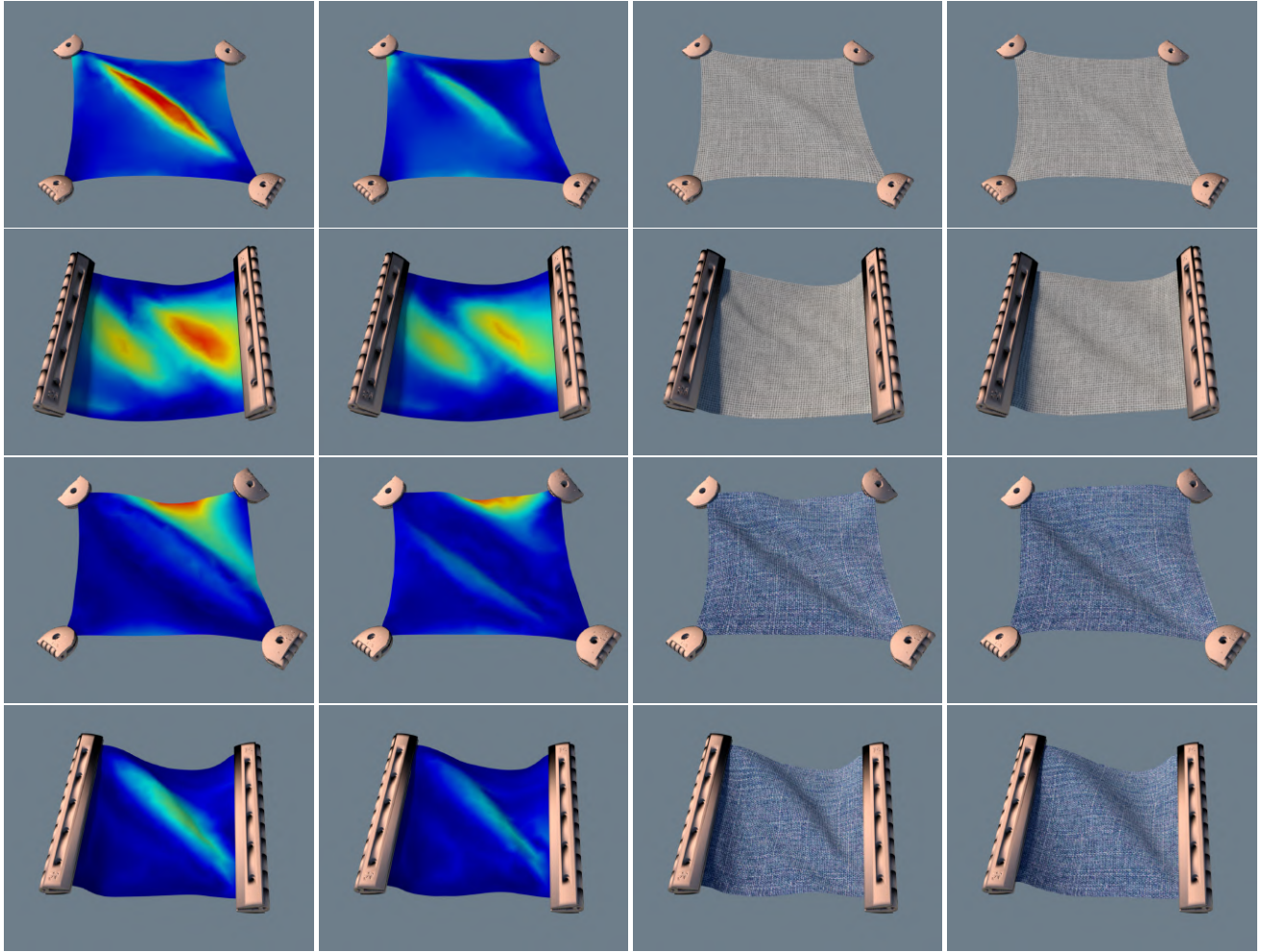


Figure 2: Evaluation of the fitting quality of our energy model on knit (top half) and denim (bottom half) cloth deformations from [MBT*12]. The first and third rows correspond to *corner-pull* motions, and the second and fourth to *complex shear*. None of them was used for training. The first column shows fitting error with a regular StVK model; the second column the error with our anisotropic, asymmetric, nonlinear model; the third column the rendered result with our model; and the fourth column the input deformation for reference. The supplementary video compares the captured frames and quasi-static simulations produced with our model. Note that quasi-static simulations may appear discontinuous in time, as each frame is solved independently.

different poses of the knee. We have posed the benchmark as the estimation of image registration between one of the poses and the rest of the poses, exploiting material estimation as the search space for image registration. The scenario constitutes a classic problem for non-rigid image registration, for which many approaches exist. However, due to the large deviation between the input images, standard methods fail, as we have attested using ITK. To avoid the problem of large initial deviations, an alternative is to first design a patient-specific FEM model, then deform the source image into the target image using this FEM model, and finally execute the registration algorithm [HHM*11].

First, we segmented the leg in the first pose and meshed it with a tetrahedral mesh (with 822 tets in our example). We then manually defined a crude correspondence between the 4 input poses (15

point correspondences in our case). We used a subset of 8 correspondences on the outer skin as boundary conditions during the fitting process, and 7 correspondences in the interior for the definition of the objective function as the sum of squared position deviations. With this crude data, we estimated a homogeneous StVK model.

Then, we progressively added material samples throughout the model (but limited to StVK, without other energy addends), until the optimization converged. For subsequent registration and material estimation steps, we defined as objective function (6) the sum of image differences between the input poses and the deformed ones. To evaluate the objective function, we rasterized the deformed tetrahedral mesh using the source volume as 3D texture map [GEP*13], and simply computed image differences w.r.t. the destination volumes for all voxels inside the tetrahedral mesh.

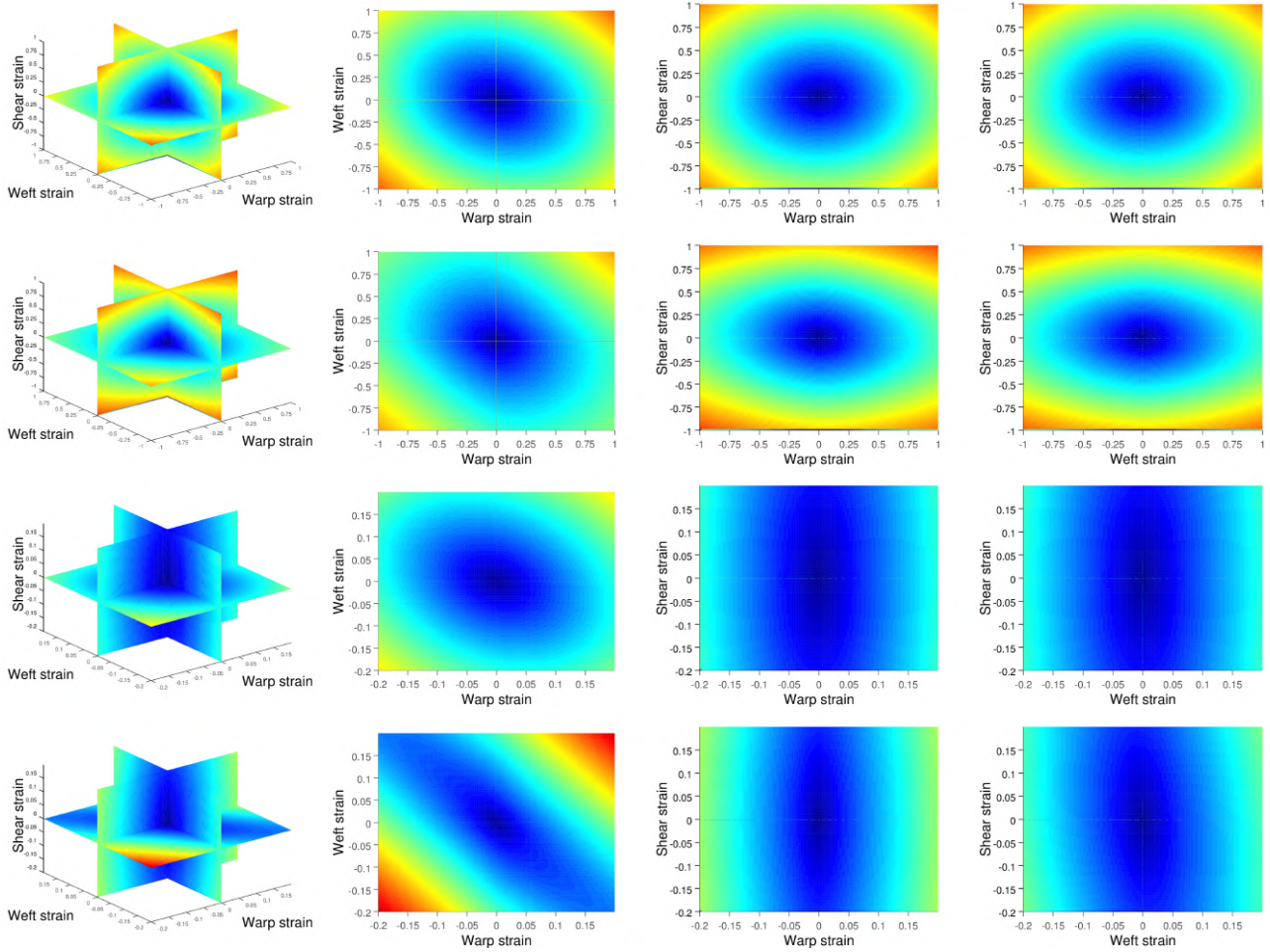


Figure 3: Visualization of strain energy functions (square-root of the energy) for knit (top half) and denim (bottom half) cloth samples. The first and third rows correspond to isotropic StVK model and the second and fourth to the final asymmetric model, including anisotropy, nonlinearities and cross-modal effects. The second to fourth columns show cross-sections of the energy function.

Knit	StVK	Aniso.	Cross.	Nonlinear	Asym.	Denim	StVK	Aniso.	Cross.	Nonlinear	Asym.
F[keys] (N)	0.3189	0.3171	0.3156	0.2944	0.2860	F[keys] (N)	2.2236	2.1616	2.1326	1.9511	1.9509
q[keys] (mm)	0.4149	0.4152	0.4051	0.4079	0.4077	q[keys] (mm)	0.5257	0.5149	0.5114	0.4827	0.4802
Obj. Func. (%)	100.00	99.123	97.349	87.856	84.097	Obj. Func. (%)	100.00	94.841	92.539	83.699	78.213
F[est] (N)	0.3189	0.3171	0.3156	0.2944	0.2860	F[est] (N)	1.6308	1.6443	1.6133	1.4401	1.4398
q[est] (mm)	0.4149	0.4152	0.4051	0.4079	0.4077	q[est] (mm)	0.5567	0.5584	0.5659	0.5322	0.5335
F[val] (N)	0.3189	0.3171	0.3156	0.2944	0.2860	F[val] (N)	0.9836	0.9548	0.9116	0.8291	0.8281
q[val] (mm)	0.4149	0.4152	0.4051	0.4079	0.4077	q[val] (mm)	1.8406	1.9859	1.8364	1.7091	1.6988

Table 2: Evolution of the fitting error for the knit and denim cloth samples as our energy model is refined. We start with a regular StVK model, and progressively add anisotropy, shear-stretch cross-stiffening, nonlinearity of unimodal energies, and asymmetry. Error is expressed as the Root Mean Square (RMS) error for forces and positions. We indicate error for the specific keyframes used for model estimation [keys], a full loading-unloading cycle from which the keyframes were extracted [est], and other deformations not used for estimation [val]. For the estimation keyframes we also indicate the error ratio w.r.t. the initial estimation with the StVK model.

Table 3 shows the improvement in RMS image error w.r.t. the homogeneous model as more material samples are progressively

added. Fig. 4 compares the input dataset with the deformation of the

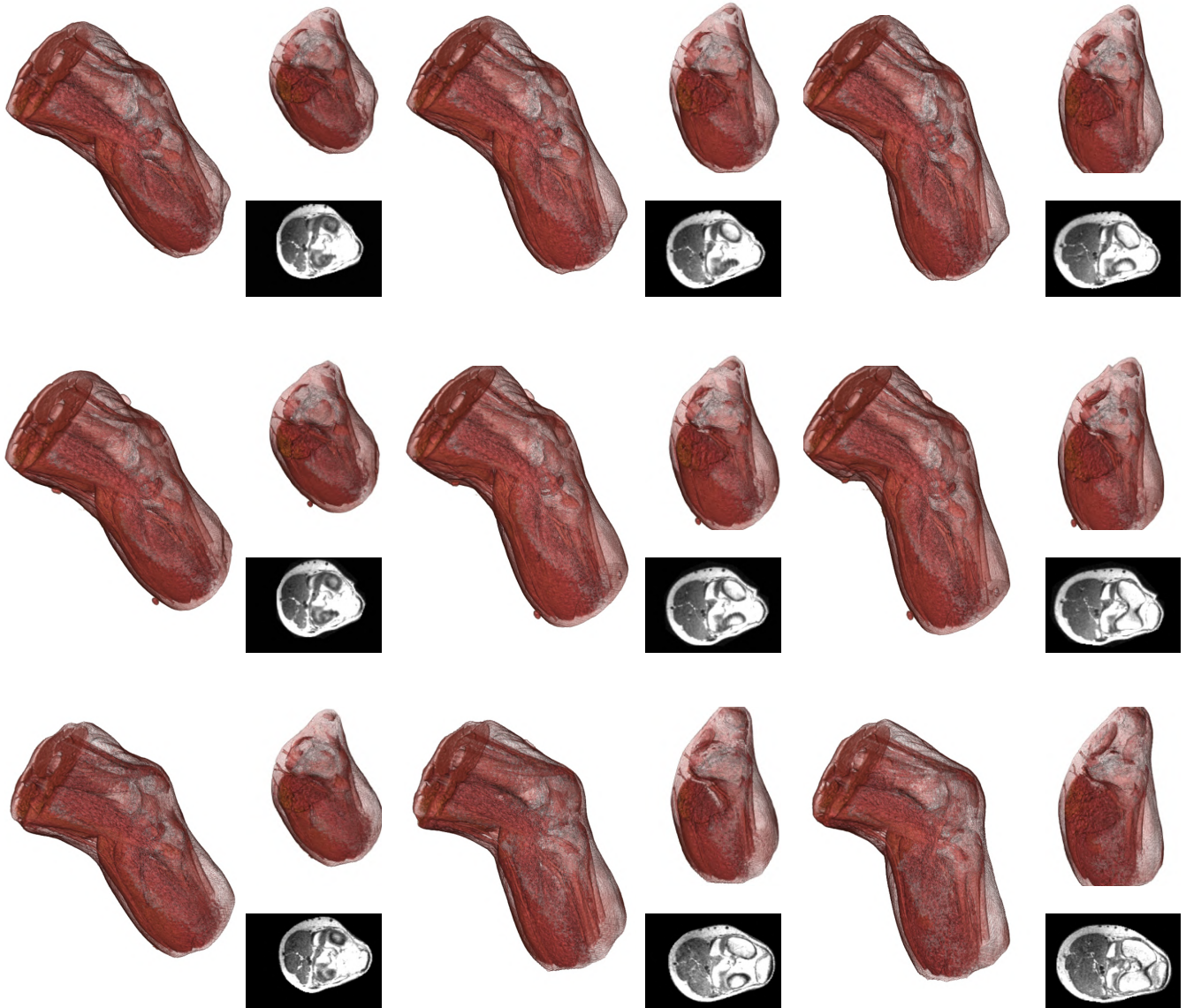


Figure 4: Evaluation of the fitting quality of our energy model on 3D MRI data of a knee from [RLNN1]. The top row shows the MRI data deformed with a homogeneous StVK model, the middle row with a heterogeneous StVK model optimized with our approach, and the bottom row the original data for reference. Along with each of the 3 poses of the knee, we show one cross-section of the dataset (both as a clipped volume and as a slice view). The small spheres in the volumetric views correspond to markers used during the scanning for knee positioning.

knee volume using the homogeneous model and our heterogeneous model with 16 material samples.

Samples	2	4	8	16
Error	96.9%	92.7%	85.1%	82.3%

Table 3: Progress of the fitting error in the knee dataset as the heterogeneity of the model is progressively refined with more material samples. The fitting error is expressed as a fraction of the fitting error with a homogeneous model.

The attached video shows the dynamic behavior of the knee in a bending scenario. With the homogeneous material the deformation is quite unrealistic, with rigid parts, such as bones, being clearly deformed. In contrast, with our heterogeneous model bones and other stiff tissues behave in a more realistic way and other common effects, such as bulges, appear.

Our results demonstrate that our energy model can successfully capture heterogeneity and reduce the fitting error. The registration results are far from optimal, but the sources of error are multiple besides possible limitations in our model. For instance, the application of boundary conditions was limited to fixing the 15 known

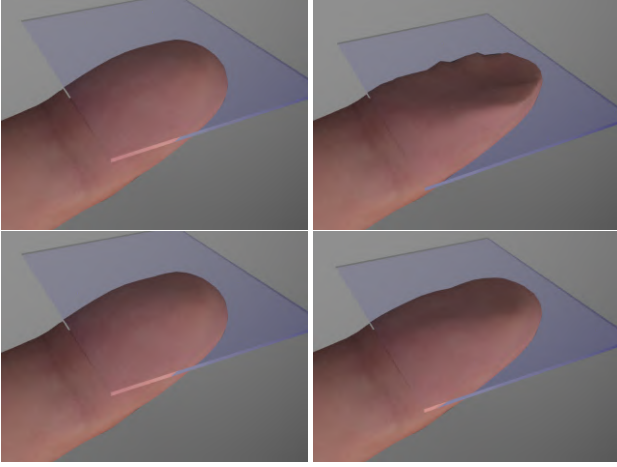


Figure 5: Simulation of a compressed finger using a regular StVK model (top) and energy-based constraints (bottom), both estimated from measured force-area data using our method. Under a force of 4 N, the StVK model collapses. With energy-based constraints, the finger exhibits the expected extreme nonlinearity of skin and is able to sustain the applied force.

correspondences on each pose. In addition, we made no assumptions about material boundaries, and the registration and material estimation could be largely improved by adding some rough segmentation of the volume.

5.3. Nonlinear Skin from Finger Pressing Experiments

Our final benchmark involves the estimation of a hyperelastic model of finger skin from controlled force-deformation data [MDC*15]. The input data, shown as red dots in Fig. 6, consists of paired values of contact area vs. total normal force for one subject's index finger pad. The data was collected keeping the subject's finger fixed, with the nail-side resting on a fixed surface, while a flat transparent moving platform was pressed against the finger pad. The platform was equipped with a force sensor, and the contact area was estimated by capturing the image of the pressed finger through the transparent platform.

In this benchmark, in particular, we have evaluated the estimation of energy-based constraints formulated in Section 3.5 to capture extreme nonlinearity. We have replicated the capture scenario, modeling the finger with a 347-tetrahedra mesh fixed on the nail area. For each of the examples, we move a fixed platform against

Model	Linear	Nonlinear	Constrained
RMS Error (N)	0.4070	0.3256	0.1749

Table 4: Evaluation of the fitting error (expressed as RMS of the contact force) for the finger experiment. We compare the error between a linear StVK material, a nonlinear material obtained by strain-dependent energy interpolation, and a linear StVK material with the addition of an energy-limiting constraint.).

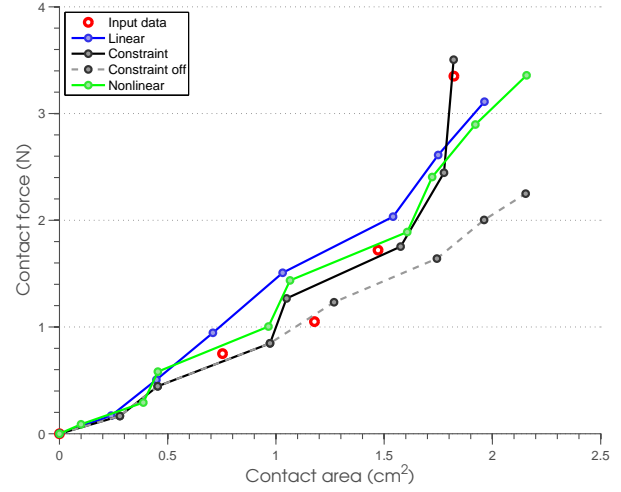


Figure 6: Plots of contact force vs. contact area for the finger dataset. The red dots indicate the input data, and the dashed lines different choices of our general energy model: (i) linear material (i.e., regular StVK), (ii) nonlinear material with strain-dependent energy interpolation, (iii) linear material with an energy-based constraint, (iv) and the linear part of the previous case (i.e., ‘Constraint off’). The energy-based constraint succeeds to capture the extreme nonlinearity in the input measurements.

the finger pad until the contact area matches the input value. We formulate the objective function as the difference between the simulated contact force on the finger pad and the input force value, and we update the model parameters as described in Section 4.2. In this benchmark, once a new set of parameters is computed, we enforce energy convexity and recalculate static equilibrium as described in Section 4, but we also reposition the moving platform for each example to match the input contact area.

We have compared the fitting error with a regular StVK model, a nonlinear material modeled using strain-dependent energy samples and cubic interpolation, and the regular StVK model with the addition of an energy-limiting constraint. The plots in Fig. 6 as well as the RMS force error shown in Table 4 clearly indicate the success of our material estimation. Interestingly, as shown in Fig. 5, our model has some additional advantages. When pressing the finger with the regular StVK model and a force of 4 N, the model collapses and tetrahedra get inverted. With energy-limiting constraints, the finger appears soft at first contact as expected, but then is capable of sustaining large forces without further deformation. Handling of tetrahedra inversion could also be added to the StVK model [ITF04].

5.4. Performance

Material optimizations of the experiments described in this section took, approximately: 24h for each cloth sample with the full energy model, 10h for the finger with the energy-limiting model, and 32h for the knee with 16 material samples. As discussed in Section 3.6, we have implemented most derivative calculations using finite differences, which hampers performance. But other steps of

the optimization also appeared as clear bottlenecks: solving static equilibrium in the cloth benchmark, simulation of constrained contact in the finger benchmark, and multiple rasterizations of volume dataset per gradient estimation in the knee benchmark.

6. Discussion and Future Work

In this paper, we have presented a general formulation of hyperelasticity based on energy addends that allows modeling and estimating various nonlinear elasticity effects in a separable manner. We couple our formulation with an optimization algorithm that enables data-driven estimation of complex hyperelasticity in diverse applications. Two of the main features of our model are the enforcement of force integrability and energy-limiting constraints, overlooked in previous approaches.

The performance of the optimization algorithm could be further improved. One of its limitations is that, in practice, we do not guarantee global enforcement of energy convexity. We enforce convexity only at discrete strain samples, for efficiency reasons. It is worth looking into simpler ways of enforcing convexity, perhaps by formulating energy addends that are convex in nature, and then global convexity could be enforced through individual convexity. Another limitation of our current enforcement of energy convexity is that convexity constraints are not satisfied implicitly during parameter updates, only through projection afterwards. The efficiency of the optimizer would increase by handling convexity constraints implicitly, as currently done for static equilibrium constraints.

The current bottleneck in the optimization is the solution of static equilibrium conditions after every parameter update. Our model would benefit from faster static equilibrium solvers, as well as more drastic minimization methods, which would reduce the number of static equilibrium solves. Concerning the optimization algorithm, one last limitation is that we rely on gradient-based optimization, which does not prevent falling in local minima. We partially avoid such local minima thanks to the incremental increase of complexity of the parameter space, but with no absolute guarantees.

In addition to hyperelasticity, the example data used in our experiments is likely to exhibit other nonlinearities, such as hysteresis. Even though modeling such nonlinear effects is orthogonal to our contribution, the fact that we do not account for them may bias the estimation of hyperelasticity in some cases.

We have demonstrated the applicability of our energy model in diverse settings, but further work would be needed to achieve more accurate results. In particular, in the medical imaging benchmark, our combined parameter estimation and registration algorithm is not at the level of specialized registration methods. We instead introduce an interesting spin to regular methods, which handle registration and model estimation as two separate tasks. For model estimation, the results could be largely improved by segmenting the data, meshing it according to the segmentation, and accounting for contact between anatomical structures. In the finger skin estimation example, the input data is rather crude, just a 1D function, hence it is insufficient for estimating an accurate skin model.

To conclude, in the future we would like to further explore the additive formulation. It would be interesting to automatically and

progressively identify and learn the best energy addends that both minimize the number of parameters and ease their estimation, while allowing simple enforcement of convexity. From a practical point of view, this would help the users in the task of choosing appropriate energy addends as well as lead to shorter estimation times and more accurate results.

Acknowledgements

We wish to thank the anonymous reviewers for their helpful comments. We also thank Taehyun Rhee for the knee data; Derek Bradley for help with the cloth data; Maria Laura D'Angelo, Matteo Bianchi and Ferdinando Cannella for the finger data; and Rosell Torres and José Miguel Espadero for help with the volume rasterization software. This work was funded in part by grants from the Spanish Ministry of Economy (TIN2012-35840), the European Research Council (ERC Starting Grant no. 280135 Animetrics), and the EU FP7 (project no. 601165 WEARHAP).

References

- [Bar88] BARNES M.: Form-finding and analysis of prestressed nets and membranes. *Computers & Structures* 30, 3 (1988), 685–695. 5
- [BBO*09] BICKEL B., BÄCHER M., OTADUY M. A., MATUSIK W., PFISTER H., GROSS M.: Capture and modeling of non-linear heterogeneous soft tissue. *ACM Trans. Graph.* 28, 3 (July 2009), 89:1–89:9. 1, 2
- [BHW94] BREEN D., HOUSE D., WOZNY M.: Predicting the drape of woven cloth using interacting particles. In *Proc. of ACM SIGGRAPH* (1994), pp. 365–372. 2
- [BJ05] BARBIĆ J., JAMES D.: Real-time subspace integration for St. Venant-Kirchhoff deformable models. *ACM Trans. Graph.* 24, 3 (Aug. 2005), 982–990. 2
- [BMF03] BRIDSON R., MARINO S., FEDKIW R.: Simulation of clothing with folds and wrinkles. *Proc. of ACM SIGGRAPH / Eurographics Symposium on Computer Animation* (2003). 2
- [BT07] BECKER M., TESCHNER M.: Robust and efficient estimation of elasticity parameters using the linear finite element method. In *SimVis* (2007), pp. 15–28. 2
- [BTH*03] BHAT K. S., TWIGG C. D., HODGINS J. K., KHOSLA P. K., POPOVIĆ Z., SEITZ S. M.: Estimating cloth simulation parameters from video. In *Proc. ACM SIGGRAPH/Eurographics SCA* (2003), pp. 37–51. 2
- [BW97] BONET J., WOOD R. D.: *Nonlinear Continuum Mechanics for Finite Element Analysis*. Cambridge University Press, 1997. 2
- [BXXBF13] BOUMAN K., XIAO B., BATTAGLIA P., FREEMAN W.: Estimating the material properties of fabric from video. In *Computer Vision (ICCV), 2013 IEEE International Conference on* (2013), pp. 1984–1991. 2
- [CDH01] CRISCIONE J. C., DOUGLAS A. S., HUNTER W. C.: Physically based strain invariant set for materials exhibiting transversely isotropic behavior. *Journal of the Mechanics and Physics of Solids* 49, 4 (2001), 871–897. 3
- [CLSM15] CHEN D., LEVIN D. I., SUEDA S., MATUSIK W.: Data-driven finite elements for geometry and material design. *ACM Transactions on Graphics (TOG)* 34, 4 (2015), 74.
- [CPS92] COTTLE R., PANG J., STONE R.: *The Linear Complementarity Problem*. Academic Press, 1992. 6
- [ESN10] EBBING V., SCHRÖDER J., NEFF P.: Construction of polyconvex energies for non-trivial anisotropy classes. In *Poly-, Quasi- and Rank-One Convexity in Applied Mechanics*, Schröder J., Neff P.,

- (Eds.), vol. 516 of *CISM International Centre for Mechanical Sciences*. Springer Vienna, 2010, pp. 107–130. 2
- [FTN11] FLYNN C., TABERNER A., NIELSEN P.: Modeling the mechanical response of in vivo human skin under a rich set of deformations. *Annals of biomedical engineering* 39, 7 (2011), 1935–1946. 2
- [GEP*13] GASCON J., ESPADERO J. M., PEREZ A. G., TORRES R., OTADUY M. A.: Fast deformation of volume data using tetrahedral mesh rasterization. In *Proceedings of the 12th ACM SIGGRAPH/Eurographics Symposium on Computer Animation* (2013), pp. 181–185. 8
- [GHDS03] GRINSPUN E., HIRANI A. N., DESBRUN M., SCHRÖDER P.: Discrete shells. In *Proceedings of the 2003 ACM SIGGRAPH/Eurographics Symposium on Computer Animation* (2003), pp. 62–67. 2, 6
- [GHF*07] GOLDENTHAL R., HARMON D., FATTAL R., BERCOVIER M., GRINSPUN E.: Efficient simulation of inextensible cloth. *Proc. of ACM SIGGRAPH* (2007). 4
- [GOH06] GASSER T. C., OGDEN R. W., HOLZAPFEL G. A.: Hyperelastic modelling of arterial layers with distributed collagen fibre orientations. *Journal of the royal society interface* 3, 6 (2006), 15–35. 2
- [HHM*11] HAN L., HIPWELL J., MERTZANIDOU T., CARTER T., MODAT M., OURSELIN S., HAWKES D.: A hybrid FEM-based method for aligning prone and supine images for image guided breast surgery. In *Biomedical Imaging: From Nano to Macro, 2011 IEEE International Symposium on* (2011), pp. 1239–1242. 7
- [ISF07] IRVING G., SCHROEDER C., FEDKIW R.: Volume conserving finite element simulations of deformable models. *Proc. of ACM SIGGRAPH* (2007). 4
- [ITF04] IRVING G., TERAN J., FEDKIW R.: Invertible finite elements for robust simulation of large deformation. *Proc. of ACM SIGGRAPH/Eurographics Symposium on Computer Animation* (2004), 131–140. 2, 10
- [Kaw80] KAWABATA S.: The standardization and analysis of hand evaluation. *Textile Machinery Soc. Japan* (1980). 2
- [KL04] KAJBERG J., LINDKVIST G.: Characterisation of materials subjected to large strains by inverse modelling based on in-plane displacement fields. *International Journal of Solids and Structures* 41, 13 (2004), 3439–3459. 3
- [KVD*02] KAUER M., VUSKOVIC V., DUAL J., SZEKELY G., BAJKA M.: Inverse finite element characterization of soft tissues. *Medical Image Analysis* 6, 3 (2002), 257–287. 3
- [LSF12] LLOYD J. E., STAVNESS I., FELS S.: Artistry: a fast interactive biomechanical modeling toolkit combining multibody and finite element simulation. In *Soft tissue biomechanical modeling for computer assisted surgery*. Springer, 2012, pp. 355–394. 3
- [MBT*12] MIGUEL E., BRADLEY D., THOMASZEWSKI B., BICKEL B., MATUSIK W., OTADUY M. A., MARSCHNER S.: Data-driven estimation of cloth simulation models. *Computer Graphics Forum (Proc. of Eurographics)* 31, 2 (may 2012). 1, 2, 6, 7
- [MDC*15] MIGUEL E., D'ANGELO M., CANNELLA F., BIANCHI M., MEMEO M., BICCHI A., CALDWELL D., OTADUY M.: Characterization of nonlinear finger pad mechanics for tactile rendering. In *World Haptics Conference (WHC), 2015 IEEE* (2015), pp. 63–68. 10
- [MEAW12] MAAS S. A., ELLIS B. J., ATESHIAN G. A., WEISS J. A.: Febio: finite elements for biomechanics. *Journal of biomechanical engineering* 134, 1 (2012), 011005. 3
- [MG04] MÜLLER M., GROSS M.: Interactive virtual materials. *Proc. of Graphics Interface* (2004). 2
- [MH83] MARSDEN J. E., HUGHES T. J. R.: *Mathematical foundations of elasticity*. Prentice-Hall civil engineering and engineering mechanics series. Prentice-Hall, 1983. 2
- [MTB*13] MIGUEL E., TAMSTORF R., BRADLEY D., SCHVARTZMAN S. C., THOMASZEWSKI B., BICKEL B., MATUSIK W., MARSCHNER S., OTADUY M. A.: Modeling and estimation of internal friction in cloth. *ACM Trans. Graph.* 32, 6 (2013), 212:1–212:10. 3
- [NSO12] NARAIN R., SAMII A., O'BRIEN J. F.: Adaptive anisotropic remeshing for cloth simulation. *ACM Trans. Graph.* 31, 6 (2012), 152:1–152:10. 2
- [Ogd97] OGDEN R. W.: *Non-Linear Elastic Deformations*. Courier Dover Publications, 1997. 2, 3
- [PCH*13] PEREZ A. G., CIRIO G., HERNANDEZ F., GARRE C., OTADUY M. A.: Strain limiting for soft finger contact simulation. *Proc. of World Haptics Conference* (2013). 4
- [PDP*15] PANOZZO D., DIAMANTI O., PARIS S., TARINI M., SORKINE E., SORKINE-HORNUNG O.: Texture mapping real-world objects with hydrographics. In *Computer Graphics Forum* (2015), vol. 34, Wiley Online Library, pp. 65–75. 3
- [PMS12] PATTERSON T., MITCHELL N., SIFAKIS E.: Simulation of complex nonlinear elastic bodies using lattice deformer. *ACM Transactions on Graphics* (2012). 2, 3
- [Pro95] PROVOT X.: Deformation constraints in a mass-spring model to describe rigid cloth behavior. *Proc. of Graphics Interface* (1995). 4
- [PvdDJ*01] PAI D. K., VAN DEN DOEL K., JAMES D. L., LANG J., LLOYD J. E., RICHMOND J. L., YAU S. H.: Scanning physical interaction behavior of 3d objects. In *Proceedings of ACM SIGGRAPH* (Aug. 2001), pp. 87–96. 2
- [RLNN11] RHEE T., LEWIS J., NEUMANN U., NAYAK K. S.: Scan-based volume animation driven by locally adaptive articulated registrations. *IEEE Transactions on Visualization and Computer Graphics* 17, 3 (2011), 368–379. 7, 9
- [SB12] SIFAKIS E., BARBIC J.: Fem simulation of 3d deformable solids: A practitioner's guide to theory, discretization and model reduction. In *ACM SIGGRAPH 2012 Courses* (2012), SIGGRAPH '12, pp. 20:1–20:50. 4
- [SLS04] SCHONER J. L., LANG J., SEIDEL H.-P.: Measurement-based interactive simulation of viscoelastic solids. *Computer Graphics Forum (Proc. Eurographics)* 23, 3 (2004), 547–556. 3
- [SSRMF06] SIFAKIS E., SELLE A., ROBINSON-MOSHER A., FEDKIW R.: Simulating speech with a physics-based facial muscle model. In *Proceedings of the 2006 ACM SIGGRAPH/Eurographics Symposium on Computer Animation* (2006), pp. 261–270. 3
- [TPBF87] TERZOPOULOS D., PLATT J., BARR A., FLEISCHER K.: Elastically deformable models. *Proc. of ACM SIGGRAPH* (1987). 2
- [TPS09] THOMASZEWSKI B., PABST S., STRASSER W.: Continuum-based strain limiting. *Computer Graphics Forum* 28, 2 (2009), 569–576. 4
- [VMT07] VOLINO P., MAGNENAT-THALMANN N.: Stop-and-go cloth draping. *Vis. Comput.* 23, 9 (2007), 669–677. 5
- [VMTF09] VOLINO P., MAGNENAT-THALMANN N., FAURE F.: A simple approach to nonlinear tensile stiffness for accurate cloth simulation. *ACM Trans. Graph.* 28, 4 (2009). 2
- [WMG96] WEISS J. A., MAKER B. N., GOVINDJEE S.: Finite element implementation of incompressible, transversely isotropic hyperelasticity. *Computer methods in applied mechanics and engineering* 135, 1 (1996), 107–128. 3
- [WOR10] WANG H., O'BRIEN J., RAMAMOORTHY R.: Multi-resolution isotropic strain limiting. *Proc. of ACM SIGGRAPH Asia* (2010). 4
- [WOR11] WANG H., O'BRIEN J., RAMAMOORTHY R.: Data-driven elastic models for cloth: Modeling and measurement. *ACM Transactions on Graphics* (2011). 1, 2
- [WWY*15] WANG B., WU L., YIN K., ASCHER U., LIU L., HUANG H.: Deformation capture and modeling of soft objects. *ACM Transactions on Graphics (TOG)* 34, 4 (2015), 94.
- [XSZB15] XU H., SIN F., ZHU Y., BARBIĆ J.: Nonlinear material design using principal stretches. *ACM Trans. on Graphics (SIGGRAPH 2015)* 34, 4 (2015). 2
- [ZYZZ] ZHANG Y., YIN C., ZHENG C., ZHOU K.: Computational hydrographic printing. *To appear in ACM TOG* 34, 4. 3